Nanoscale

PAPER

View Article Online
View Journal | View Issue

Check for updates

Cite this: *Nanoscale*, 2017, **9**, 18268

Super-resolution imaging by metamaterial-based compressive spatial-to-spectral transformation†

Qian Ma, ‡[a] Huan Hu,‡[a] Eric Huang[b] and Zhaowei Liu*[a]

Received 25th July 2017,
Accepted 30th October 2017

DOI: 10.1039/c7nr05436j

rsc.li/nanoscale

We present a new far-field super-resolution imaging approach called compressive spatial to spectral transformation microscopy (CSSTM). The transformation encodes the high-resolution spatial information to a spectrum through illuminating sub-diffraction-limited and wavelength-dependent patterns onto an object. The object is reconstructed from scattering spectrum measurements in the far field. The resolution of the CSSTM is mainly determined by the materials used to perform the spatial to spectral transformation. As an example, we numerically demonstrate sub-15 nm resolution by using a practically achievable Ag/SiO_2 multilayer hyperbolic metamaterial.

I. Introduction

The achievable spatial resolution of a conventional optical microscope, also known as the diffraction limit, is about one half of the wavelength of the light. Currently, there are three general strategies to beat this limit and achieve super-resolution in a fluorescence microscope: single fluorophore localization[1] (*e.g.* stochastic optical reconstruction microscopy (STORM),[2] photo-activated localization microscopy (PALM)[3,4] and point accumulation for imaging in nanoscale topography (PAINT)[5]), point spread function engineering (*e.g.* stimulated emission depletion (STED)[6,7]), and structured illumination.[8,9] Despite the enormous advances,[10] these techniques still use diffraction-limited optics and inevitably require trade-offs in other imaging characteristics, such as speed, phototoxicity, versatility, or the field of view to reach these resolutions. For instance, localization-based technology typically can achieve 10–20 nm resolution, but requires a relatively long time to identify a sufficient number of fluorophores from thousands of camera frames. When both temporal resolution and spatial resolution are needed, structured illumination microscopy (SIM) stands out since it only requires a few camera frames to reconstruct one super-resolution image. The resolution of linear SIM has been demonstrated as high as 84 nm (ref. 11) along with a reported frame rate of ~14 Hz.[12] By shrinking the size of structured patterns, plasmonic structured illumination microscopy (PSIM)[13,14] or localized plasmon assisted structured illumination microscopy (LPSIM)[15] can further bring the resolution down to a 50 nm scale without reducing the imaging speed.

In contrast to conventional diffraction-limited optics, the use of plasmonics and metamaterials introduces the capability to manipulate light at sub-diffraction scales.[16] This is due to the ability of metamaterials to allow high spatial-frequency waves that are typically evanescent in air to propagate. Thus, utilizing plasmonics and metamaterials provides alternative strategies for super-resolution imaging, which is also not necessarily limited to fluorescence imaging. First theorized in the form of Pendry's perfect lens,[17] many hyperlenses[18,19] or metalenses[20,21] have since been proposed and demonstrated. These hyperlenses or metalenses act like a conventional lens, but possess much higher resolving power. In the case of a hyperlens,[18] a magnified image of a high-resolution object is formed in the far field. The resolution of a hyperlens, in theory, can be at the sub-10 nm scale,[22] determined by the highest spatial-frequency wave the material can carry. However, due to its limited physical size and curved geometry, it has a limited field of view. Although a transformation optics based flat-hyperlens has been proposed, it hasn't been demonstrated experimentally due to material fabrication challenges.[23,24] Recently, the development of an all-dielectric metamaterial superlens has shown its potential in enlarging the field of view and lowering the losses.[25]

Besides lens-based approaches, metamaterials can also work with computational imaging methods. An example of this was studied at radio frequency:[26] a metamaterial is used to create wavelength-dependent sampling patterns, and an object is firstly sampled by these patterns and is then reconstructed by an algorithm known as compressive sensing.[27] Recently, a theoretical study of hyper-structured illumination[28]

[a]*Department of Electrical and Computer Engineering, University of California San Diego, La Jolla, California 92093, USA. E-mail: zhaowei@ucsd.edu*
[b]*Department of Physics, University of California San Diego, La Jolla, California 92093, USA*

†Electronic supplementary information (ESI) available. See DOI: 10.1039/c7nr05436j

‡These authors contributed equally to this work.

was reported which brings the idea of structured illumination and hyperbolic metamaterials (HMMs) at optical frequency together to allow a planar geometry and in principle an unlimited field of view. Nevertheless, to achieve a 2-dimensional sub-diffraction-limited image by using a planar HMM for a practically achievable design remains elusive.

In this letter, we propose a metamaterial-based reconstructive super-resolution imaging approach, called compressive spatial to spectral transformation microscopy (CSSTM). The basic working principle of CSSTM follows a few steps: firstly, an optical metamaterial is used to generate near field, sub-diffraction-limited illumination patterns. These patterns are changed by sweeping the input wavelength. Secondly, an object close to the metamaterial surface is illuminated/sampled by a series of these deep sub-wavelength patterns and scatters light into the far field. Thirdly, by collecting the total output intensity at each wavelength in the far field, the 2D spatial information of the object is successfully encoded into a 1D spectral pattern (Fig. 1b). The spatial to spectral transformation can be generally described by:

$$S(\lambda) = \iint H(x, y, \lambda) O(x, y) \mathrm{d}x \mathrm{d}y, \quad (1)$$

where S is the spectrum, O is the object, and H is a series of illumination patterns at different wavelengths λ. Finally, the object is reconstructed through a sparse-based algorithm[29,30] by using the known illumination patterns.

The resolution of CSSTM is mainly determined by the resolution of illumination patterns, which is the highest spatial-frequency wave a metamaterial can carry. We present a numerical example of using a practical flat hyperbolic Ag/SiO_2 multilayer. Our simulation results show that the reconstructed image can resolve the object with a resolution as high as 12 nm, using the obtained spectral information from 400 nm to 1.2 μm. The reconstruction algorithm is also known as compressive sensing, which can reconstruct an object through a limited number of measurements. Thus, it reduces the total number of wavelength channels. We then discuss the working conditions of this approach under various sparse conditions of the object, desired resolutions, and SNR conditions. We believe that CSSTM provides an alternative solution for super-resolution imaging. Because it does not require extra measurements for one super-resolution image (a spectrum can be measured through a single shot of camera frame, or even faster through pulse-stretching methods[31]), this technology can also be potentially useful for high speed image recording.[32]

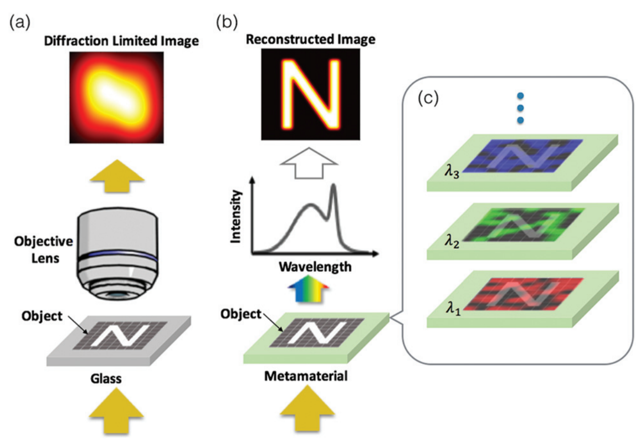

Fig. 1 The concept of the compressive spatial-to-spectral transformation microscopy (CSSTM). (a) Diffraction-limited image acquired by a conventional objective lens. (b) Sub-diffraction-limited image reconstructed from the metamaterial-based spatial-to-spectral transformer. High-resolution spatial information is transformed into the spectral domain by projecting a series of wavelength-dependent illumination patterns as shown in (c) onto the object.

II. Results & discussion

Dispersion properties of hyperbolic metamaterials

We take advantage of highly dispersive HMMs to generate wavelength-dependent illumination patterns. This is done by simulating alternating layers of thin films Ag and SiO_2 with thicknesses far below the operating wavelength. The stacked thin films can be approximated by effective medium theory (EMT) and the dispersion relation of HMMs can be written as:

$$\frac{k_x^2}{\varepsilon_z} + \frac{k_z^2}{\varepsilon_x} = \frac{\omega^2}{c^2}, \quad (2)$$

where $\varepsilon_z > 0$ and $\varepsilon_x > 0$ (we ignore the y direction contribution due to symmetry).

The isofrequency curves in the k_x and k_z plane are plotted in Fig. 2a. The hyperbolic curve indicates that all the high-k modes have almost the same group velocity direction. Therefore, the in-coupled beam won't diverge when it propagates inside the HMM. In addition, the group velocity direction is wavelength-dependent, so that light with different wavelengths illuminates different locations on the top of the HMM surface, respectively. This phenomenon can be clearly identified from the two-dimensional simulation results as shown in Fig. 2b and c, where the in-coupled light through a 10 nm slit in a Cr mask is split into two beams with well-defined directions and widths. This special property of HMMs has been used for applications such as nanolithography.[33] Here, we use the FWHM of the beam on the top of the HMM surface to qualitatively state the finest resolution of illumination patterns. The FWHM is determined by the unit cell size of the HMM, the slit's width and intrinsic material losses.

In this letter, we use effective medium theory to predict the performance of our CSSTM system. With approximation of effective medium theory, the beam has a FWHM ∼ 20 nm at 500 nm when the total thickness of the HMM is 130 nm. The FWHM becomes ∼27 nm when the thickness of the HMM increases to 250 nm due to material loss.

It is worth noting that the unit cell size of the HMM also affects the FWHM in practice. A supplementary plot (Fig. S1†)

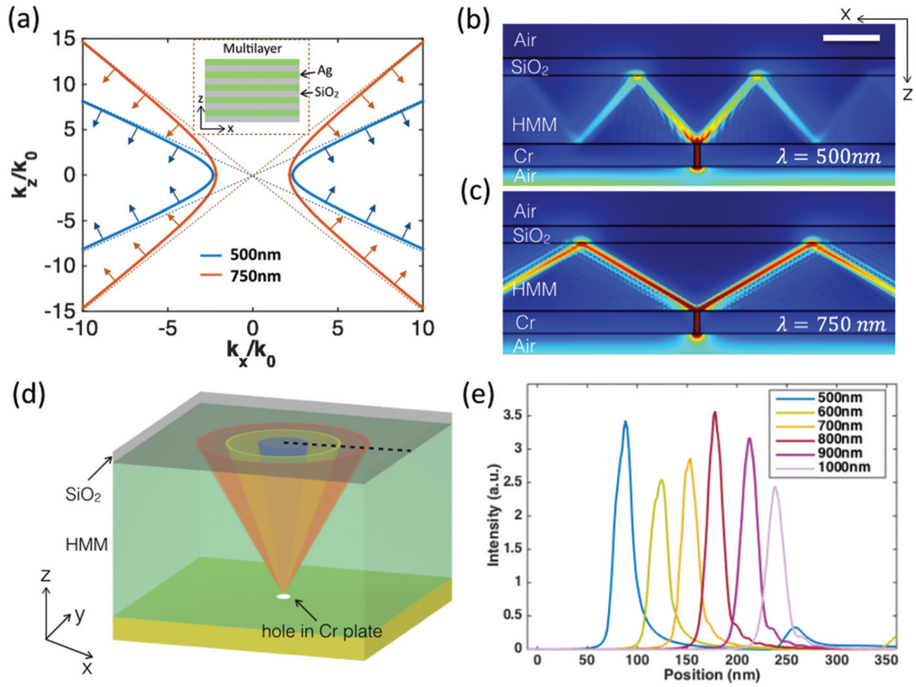

Fig. 2 The dispersive hyperbolic metamaterial (HMM) for the spatial-to-spectral transformation (CSST). (a) Isofrequency contours show that light of different wavelengths propagates along different directions inside of the HMMs. (b) (c) Full wave simulation of the electric field in the HMM. Scale bar: 100 nm. (d) Schematic illustration of the concentric rainbow formation on the top surface of the HMM. Broadband non-polarized light is coupled into the HMM through a hole in a Cr layer. (e) 1D plot of intensity along the dashed line in (d) (at 1 nm above the HMM and SiO_2 interface). The 1 : 1 Ag/SiO_2 multilayer HMM (250 nm thickness) is calculated using effective medium theory.

shows the FWHM *versus* different sizes of the unit cells of the HMM. A recent experiment on multilayer HMMs has improved the unit cell size to a sub-10 nm scale.[34]

In a three-dimensional geometry, when a broadband plane wave (non-polarized) is normally incident on the HMM through a small hole (~10 nm diameter), the pattern generated on the output surface of the HMM is expressed as a concentric rainbow (Fig. 2d). The larger the wavelength, the larger the radius of the ring, but with ~20 nm ring thickness (see Fig. 2e) for each single wavelength. Therefore, a 1-to-1 mapping between the wavelength and the ring diameter is formed.

Spatial to spectral transformation

Linking the wavelength with the illumination ring diameter only provides 1D spatial information. To obtain a 2D spatial image, we intuitively put multiple nanoholes (~10 nm in diameter and 20 of them in this specific example) on the bottom of the HMM, as schematically shown in Fig. 3a. To make sure that each pixel in an image has a unique encoded spectrum, the mutual coherence of the transformation matrix H in eqn (1) is used to quantitatively state the maximum coherence of the encoded spectrum for any two pixels.[35] It takes multiple trials to obtain a good distribution for all the holes (Fig. 3b). An object is placed on the surface of the HMM, which scatters the near field light into the far field. To simplify the process without losing the essence in physics, the wavelength-dependence of scattering is ignored in this simulation but should be calibrated and corrected in practice. Based on this assumption, the transformation matrix $H(x_i,y_i;\ \lambda)$ could be calculated *via* simulating illumination patterns for all wavelengths (Fig. 3c). Fig. 3d shows two exemplary illumination patterns at two selected wavelengths. Each pixel shown in Fig. 3d has a unique encoded spectrum from 400 nm to 1200 nm (Fig. 3e).

Since the illumination pattern is also polarization dependent, one could also add two polarization states (x-polarized and y-polarized) in the transformation to increase the total number of measurements. The sets of all illumination patterns with respect to both wavelength and polarization are illustrated by two movies (Movies 1 and 2) in the ESI.†

Let's now divide the imaging area into $N \times N$ pixels. The physical size of each pixel is deep sub-diffraction limited. The object is represented as $O(x_i,y_i)$ and the illumination pattern at wavelength λ is represented as $H(x_i,y_i,\lambda)$. Assume that a linear interaction occurred between the object and illumination patterns, then the detected total light intensity in the far field at a certain wavelength is

$$I(\lambda) \approx \Delta x \Delta y \sum_{i,j=1}^{N} O(x_i, y_j) H(x_i, y_j, \lambda) \tag{3}$$

Reshape $O(x_i,y_i)$ to a vector with size $N^2 \times 1$ and $H(x_i,y_j,\lambda)$ to a matrix with size $M \times N^2$, where M is the number of measurements (*i.e.* wavelength channels), and Δx and Δy are the physical size of a pixel.

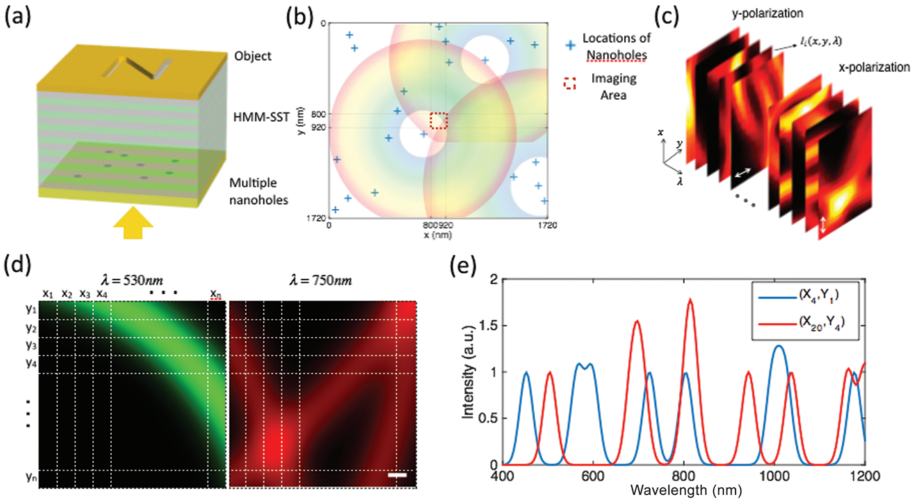

Fig. 3 The implementation of CSSTM for 2D imaging. (a) Schematic of a HMM spatial to spectral transformer (SST). Multiple nanoholes are randomly distributed in a Cr photomask attached to the bottom of a HMM slab. (b) Distribution of 20 nanoholes and the location of the measured object area. Each nanohole forms a circular, rainbow-like illumination pattern overlapping with the object. (c) Dataset of transformation: a stack of illumination patterns controlled by both the wavelength and polarization. Wavelength: 400 nm–1200 nm. Polarization: x-polarized and y-polarized. (d) Two examples of illumination patterns within the red dotted area in (b) generated by non-polarized light at 500 nm (Left) and 750 nm (Right), respectively. Scale Bar: 10 nm. (e) Encoded spectra from 400 nm to 1200 nm of two exemplary pixels [(X_4, Y_1); (X_{20}, Y_4)] in (d).

Now we can re-write the equation in a matrix form

$$I_{M\times 1} \approx H_{M\times N^2} \cdot O_{N^2\times 1} \tag{4}$$

The effective measurement number M is limited by the number of wavelength channels. M is typically smaller than N^2 in any k-space limited system. Thus, these linear equations cannot be directly solved. We use compressive sensing algorithms to find a near-optimal estimation $\hat{O}$ of solution O with a limited number of measurements M by assuming that the object is sparse.

Imaging reconstruction

We firstly study the sparse-based reconstruction under ideal conditions. A pixelated binary UCSD library logo (Fig. 4a) is sampled *via* a series of illumination patterns (Fig. S2(a–f)†) from 400 nm to 1200 nm with two linear polarization (x-polarized and y-polarized) plane waves. The physical size of each

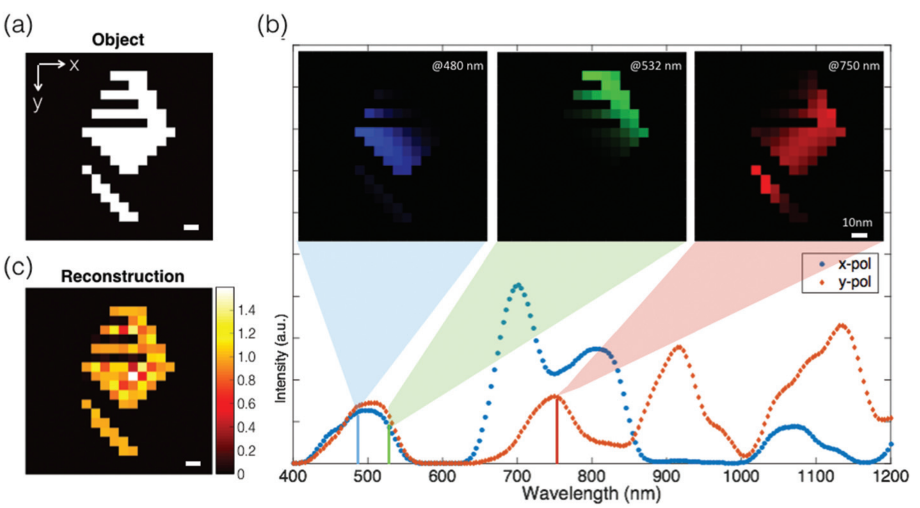

Fig. 4 CSSTM reconstruction result under ideal conditions. (a) Test object. A simplified UCSD logo is pixelated to 20 by 20 pixels. Physical size per pixel: 6 nm. (b) Simulated spectrum in the far field under two orthogonal incident polarizations. Each data point in the spectra represents the summation of the intensity in the far field at a given wavelength and polarization. Three sub-images in (b) show part of the object illuminated at wavelengths 480 nm (x-polarization), 532 nm (x-polarization) and 750 nm (y-polarization), respectively. A spectrum has 200 wavelength channels. (c) Reconstructed image with high fidelity and resolution. Scale bar: 10 nm.

pixel is set to be 6 nm, smaller than half of the smallest FWHM of the illumination patterns (~27 nm). Apparently, the deep sub-wavelength object won't be directly resolved in the far field (Fig. S2(g–i)†), but the high spatial resolution information is encoded into the spectrum (Fig. 4b). The reconstruction is carried out through the l1_ls algorithm.[29] During reconstruction, we found out that if an object is known to be sparse, the reconstruction code tends to end up with a higher resolution image compared to the illumination patterns. For instance, the reconstructed result in Fig. 4c can resolve two lines with 12 nm separation. We consider this as another advantage of compressive sensing, which uses a prior knowledge of object sparsity and extrapolates the detecting bandwidth in reconstruction.[36]

We then explore if the reconstruction is robust to noise. Because we used a sparse-based algorithm, the result also depends on the accuracy of the sparsity-constraint. Qualitatively speaking, reconstruction is more robust to noise when an object is sparse (fewer non-zero values). For instance, Fig. S3† shows the reconstruction results of two objects with different numbers of non-zeroes. One object contains only two non-zero pixels (out of 400 unknowns), while the other object contains ten non-zero pixels which form a 'smiling' face. Both images are reconstructed when the SNR is 30 dB. The 'smiling' face starts to fail when the SNR falls to 20 dB, and the 'two dots' start to fail when the SNR is 10 dB. Fig. 5 shows the reconstruction accuracy *versus* object sparsity and SNR. The reconstruction accuracy is defined as

$$C = \frac{\sum_{x,y}\{\mathrm{Image}(x,y)\cdot\mathrm{Object}(x,y)\}}{\sum_{x,y}\mathrm{Image}(x,y)\sum_{x,y}\mathrm{Object}(x,y)}, \tag{5}$$

The reconstruction accuracy fails quickly when either the object sparsity or SNR reaches a certain barrier. If we define a threshold for the reconstruction accuracy, the iso-accuracy contour in Fig. 5 stands for a working window of this method.

It should be emphasized that the illumination pattern significantly affects the resolution of our CSSTM system. The smaller the features of the illumination patterns are, the higher the resolution of the object tends to be reconstructed. In addition, our reconstruction results have higher resolution than the illumination pattern, even under noisy signal conditions. We understand this as a benefit of spatial frequency bandwidth extrapolation induced by compressive sparsity-based reconstruction.[36] Like other extrapolation processes, whether a reconstruction will be successful is highly dependent on the noise level and the accuracy of the sparsity constraints.

Therefore, the final resolution of the CSSTM is ultimately determined by the achievable bandwidth (a half of the pixel spatial frequency of the reconstructed image) with high fidelity after the reconstruction. Based on the results shown in Fig. 4, the resolution of CSSTM is ~2 times better than that of the illumination patterns generated by the HMM-based spatial-to-spectral transformer.

The trade-offs between the image size, the sparsity of the object and the imaging resolution (or pixel size) are linked by the following relationship:[27]

$$M \geq C\cdot\mu^2(H)\cdot S\cdot\log(n), \tag{6}$$

where M is the total number of effective measurements, μ is the mutual coherence of the sensing matrix H in eqn (3), S is the number of nonzero elements in the reconstruction basis, n is the total number of unknowns, and C is a constant.

For a given transformation mentioned above, the mutual coherence μ is related to the pixel size. A large pixel size decreases the similarity of the encoded spectrum of any two adjacent pixels. Thus, it results in a smaller μ, and allows for the reconstruction of a less sparse object. However, the imaging resolution must be sacrificed accordingly. On the other hand, an increase in n means making a larger field of view without changing the pixel size, but it requires either a smaller S or a larger M for a successful reconstruction. Therefore, based on what the actual sample would be, one may need to find suitable working conditions by tuning these parameters.

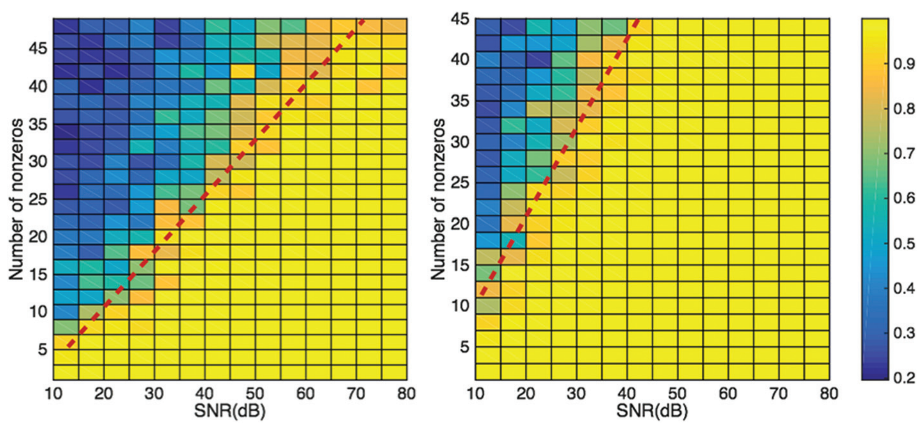

Fig. 5 Reconstruction accuracy *versus* signal noise ratio and sparsity. Left: Pixel size: 6 nm; field of view: 120 nm × 120 nm; right: Pixel size 10 nm; field of view: 200 nm × 200 nm. The right side of the red dashed line is considered as accurate reconstructions.

III. Conclusions

We explored the possibility of using metamaterials as a super-resolution compressive sensing imager. We proposed a super-resolution approach named compressive spatial to spectral transformation microscopy (CSSTM), through which the super-resolution spatial information is encoded into the spectral domain and then retrieved by a sparse-based reconstruction algorithm. Concept-proof simulation results are provided to demonstrate the capability of this CSSTM method. One exemplary design of the CSSTM shows successful image reconstruction with 12 nm resolution and a field of view of 120 nm × 120 nm by utilizing 200 wavelength channels from 400 nm to 1200 nm. This approach is robust to noise when the object is sparse.

In contrast to other super-resolution technologies, the HMM-based CSSTM performs high-resolution scattering imaging based on a single shot spectrum (or two if two polarizations are used). This principle may also apply to fluorescence imaging but it requires that the illumination spectrum can be fitted into the fluorescence absorption band. Without the cost of large numbers of measurements, we believe that CSSTM is also beneficial when both temporal and spatial resolution are required.

The metamaterial utilized in this work has a flat geometry, which makes it possible to adapt wide-field imaging. However, one challenge in wide-field imaging is to get enough measurements for the increased number of object unknowns when its field of view becomes larger. One potential solution is to acquire diffraction-limited spectral images in the far field. Then, each diffraction limited zone could be treated as a single-shot-spectrum imager to reconstruct a high-resolution image.

The CSSTM system implements an existing, practically achievable Ag/SiO_2 material system. The geometrically patterned nanoholes can be made by existing nanofabrication tools such as electron beam lithography or focused ion beam. A calibration process of the illumination patterns might be necessary when either the positioning of nanoholes or the material property of the HMM is not accurate. The calibration can be performed by high resolution NSOM measurement on the HMM surface to extract near field patterns with respect to various operation frequencies.

Conflicts of interest

The authors declare no competing financial interest.

Acknowledgements

H. Qian, A. Bezryadina, J. Ponsetto and Y. Han are warmly thanked for valuable discussions. This work is supported by Gordon and Betty Moore Foundation.

References

1 G. Patterson, M. Davidson, S. Manley and J. Lippincott-Schwartz, *Annu. Rev. Phys. Chem.*, 2010, **61**, 345–367.
2 M. J. Rust, M. Bates and X. Zhuang, *Nat. Methods*, 2006, **3**, 793–796.
3 E. Betzig, G. H. Patterson, R. Sougrat, O. W. Lindwasser, S. Olenych, J. S. Bonifacino, M. W. Davidson, J. Lippincott-Schwartz and H. F. Hess, *Science*, 2006, **313**, 1642–1645.
4 S. T. Hess, T. P. K. Girirajan and M. D. Mason, *Biophys. J.*, 2006, **91**, 4258–4272.
5 A. Sharonov and R. M. Hochstrasser, *Proc. Natl. Acad. Sci. U. S. A.*, 2006, **103**, 18911–18916.
6 S. W. Hell and J. Wichmann, *Opt. Lett.*, 1994, **19**, 780.
7 T. A. Klar and S. W. Hell, *Opt. Lett.*, 1999, **24**, 954–956.
8 M. G. L. Gustafsson, *Proc. Natl. Acad. Sci. U. S. A.*, 2005, **102**, 13081–13086.
9 L. Schermelleh, P. M. Carlton, S. Haase, L. Shao, L. Winoto, P. Kner, B. Burke, M. C. Cardoso, D. A. Agard, M. G. L. Gustafsson, H. Leonhardt and J. W. Sedat, *Science*, 2008, **320**, 1332–1336.
10 F. Balzarotti, Y. Eilers, K. C. Gwosch, A. H. Gynnå, V. Westphal, F. D. Stefani, J. Elf and S. W. Hell, *Science*, 2017, **355**, 606–612.
11 D. Li, L. Shao, B.-C. Chen, X. Zhang, M. Zhang, B. Moses, D. E. Milkie, J. R. Beach, J. A. Hammer, M. Pasham, T. Kirchhausen, M. A. Baird, M. W. Davidson, P. Xu and E. Betzig, *Science*, 2015, **349**, aab3500.
12 M. Shaw, L. Zajiczek and K. O'Holleran, *Methods*, 2015, **88**, 11–19.
13 F. Wei and Z. Liu, *Nano Lett.*, 2010, **10**, 2531–2536.
14 F. Wei, D. Lu, H. Shen, W. Wan, J. L. Ponsetto, E. Huang and Z. Liu, *Nano Lett.*, 2014, **14**, 4634–4639.
15 J. L. Ponsetto, F. Wei and Z. Liu, *Nanoscale*, 2014, **6**, 5807–5812.
16 D. Lu and Z. Liu, *Nat. Commun.*, 2012, **3**, 1205.
17 J. B. Pendry, *Phys. Rev. Lett.*, 2000, **85**, 3966–3969.
18 Z. Liu, H. Lee, Y. Xiong, C. Sun and X. Zhang, *Science*, 2007, **315**, 1686.
19 J. Rho, Z. Ye, Y. Xiong, X. Yin, Z. Liu, H. Choi, G. Bartal and X. Zhang, *Nat. Commun.*, 2010, **1**, 143.
20 F. Lemoult, G. Lerosey, J. De Rosny and M. Fink, *Phys. Rev. Lett.*, 2010, **104**, 203901.
21 C. Ma and Z. Liu, *J. Nanophotonics*, 2011, **5**, 51604.
22 B. Wood, J. B. Pendry and D. P. Tsai, *Phys. Rev. B: Condens. Matter*, 2006, **74**, 115116.
23 S. Han, Y. Xiong, D. Genov, Z. Liu, G. Bartal and X. Zhang, *Nano Lett.*, 2008, **8**, 4243–4247.
24 A. V. Kildishev and V. M. Shalaev, *Opt. Lett.*, 2008, **33**, 43–45.
25 W. Fan, B. Yan, Z. Wang, *et al.*, *Sci. Adv.*, 2016, **2**, e1600901.
26 J. Hunt, T. Driscoll, A. Mrozack, G. Lipworth, M. Reynolds, D. Brady and D. R. Smith, *Science*, 2013, **339**, 310–313.
27 E. J. Candes and M. B. Wakin, *IEEE Signal Process Mag.*, 2008, **25**, 21–30.

28 E. Narimanov, *ACS Photonics*, 2016, **3**, 1090–1094.
29 S. B. Kwangmoo Koh and S.-J. Kim, *J. Mach. Learn. Res.*, 2007, **8**, 1519–1555.
30 J. M. Bioucas-Dias and M. A. T. Figueiredo, *IEEE Trans. Image Process.*, 2007, **16**, 2992–3004.
31 K. Goda and B. Jalali, *Nat. Photonics*, 2013, **7**, 102–112.
32 E. Huang, Q. Ma and Z. Liu, *Sci. Rep.*, 2016, **6**, 25240.
33 S. Ishii, A. V. Kildishev, E. Narimanov, V. M. Shalaev and V. P. Drachev, *Laser Photonics Rev.*, 2013, **7**, 265–271.
34 H. Shen, D. Lu, B. VanSaders, J. J. Kan, H. Xu, E. E. Fullerton and Z. Liu, *Phys. Rev. X*, 2015, **5**, 21021.
35 M. F. Duarte, M. A. Davenport, D. Takhar, J. N. Laska, K. F. Kelly and R. G. Baraniuk, *IEEE Signal Process Mag.*, 2008, **25**, 83–91.
36 A. Szameit, Y. Shechtman, E. Osherovich, E. Bullkich, P. Sidorenko, H. Dana, S. Steiner, E. B. Kley, S. Gazit, T. Cohen-Hyams, S. Shoham, M. Zibulevsky, I. Yavneh, Y. C. Eldar, O. Cohen and M. Segev, *Nat. Mater.*, 2012, **11**, 455–459.